analytica

MDPI

Article

Interpretable Chemometric Modeling of Azo Dye Adulteration in Paprika Powder by Benchtop FT-NIR and Handheld Vis-NIR Spectroscopy

Justyna Grabska, Krzysztof B. Bec *, Vanessa Moll, Anna Fiegl-Lechner and Christian W. Huck

Institute of Analytical Chemistry and Radiochemistry, CCB—Center for Chemistry and Radiochemistry, Leopold-Franzens University, Innrain 80-82, 6020 Innsbruck, Austria; justyna.grabska@uibk.ac.at (J.G.); a.fiegl@student.uibk.ac.at (A.F.-L.); christian.w.huck@uibk.ac.at (C.W.H.)

* Correspondence: krzysztof.bec@uibk.ac.at

Abstract

Synthetic azo dyes are relevant paprika adulterants and a food-safety concern when used in undeclared or non-authorized forms. This study investigated the quantification of three representative dyes—Allura Red (E129), Orange II, and Ponceau 4R (E124)—spiked into paprika powder from 0 to 6% *w*/*w* using a benchtop Fourier-transform NIR (FT-NIR) Büchi NIRFlex N-500 spectrometer and a handheld ASD QualitySpec Trek Vis-NIR spectrometer. The experimental design included 17 concentration levels per dye, 3 independently prepared spiked batches per level, randomized measurements over approximately 3 months, and 3 replicate spectral acquisitions per filled cuvette. Measurements were performed in the 10,000–4000 cm^{-1} region with the benchtop FT-NIR instrument and in the 20,408–4000 cm^{-1} region with the handheld Vis-NIR instrument. Spectra were evaluated by principal component analysis (PCA) and partial least squares (PLS) regression, with robustness assessed by grouped cross-validation and independent test-set validation using held-out concentration levels. To support model interpretation, anharmonic NIR spectra of the dyes were simulated using DVPT2 calculations and compared with the experimentally relevant loading regions. For FT-NIR, independent test-set validation gave RMSEP values of 0.315, 0.205, and 0.338% *w*/*w* and R^2_{TSV} values of 0.970, 0.987, and 0.965 for Allura Red, Orange II, and Ponceau 4R, respectively. For Vis-NIR, the corresponding RMSEP values were 0.328, 0.262, and 0.334% *w*/*w*, with R^2_{TSV} values of 0.968, 0.979, and 0.964. The models required only two to three latent variables. Orange II gave the strongest FT-NIR model, reflecting its more distinct NIR spectral response, while all Vis-NIR models remained compact two- to three-factor models due to the additional visible-region absorption of the azo chromophores. The simulated spectra supported assignment of the main FT-NIR model-relevant regions to aromatic C–H overtones and dense combination-band manifolds, while the Vis-NIR models were driven mainly by visible chromophore absorption.

Keywords: paprika adulteration; azo dyes; NIR spectroscopy; Vis-NIR spectroscopy; PLS regression; food authentication

Academic Editor: Maria Luisa Astolfi

Received: 17 July 2026
Revised: 14 August 2026
Accepted: 26 August 2026
Published: 28 August 2026

1. Introduction

Authentication and adulteration control in foods remain important because declared quality and consumer safety can be compromised by undeclared additives, substitution, dilution, or masking of inferior raw materials [1]. A recurring form of economically motivated adulteration is the addition of synthetic dyes to intensify or restore the visual appearance of

natural products. Ground paprika is especially vulnerable to this practice because color is a major quality attribute and directly affects consumer perception and commercial value. The characteristic red color of paprika originates mainly from carotenoids, especially capsanthin and capsorubin, whose content and visual intensity can decrease during processing and storage [2]. This creates an incentive to compensate for color loss by adding undeclared or non-authorized colorants. Importantly, the regulatory status of synthetic dyes differs: Allura Red (E129) and Ponceau 4R (E124) are authorized food colorants under defined conditions and intake restrictions, while other azo dyes are not authorized for food use; European Food Safety Authority (EFSA) re-evaluations provide the toxicological basis for the regulated use of E129 and E124 [3,4].

Paprika and chili powder have repeatedly been identified as risk matrices in spice fraud. European spice supply chains are long and largely import-dependent, increasing the number of points at which substitution, dilution, or color enhancement may occur [5]. In the EU coordinated control plan on herbs and spices, 462 paprika/chili samples were analyzed; 27 were considered suspicious, and non-authorized dyes were detected in 10 samples, corresponding to 2.2% of the paprika/chili subset [6,7]. Reported adulteration practices include the addition of synthetic dyes, replacement with spent paprika or other plant material, and mineral extenders that alter ash content [7–9]. Historically, much attention has focused on industrial azo dyes such as Sudan dyes, which triggered regulatory actions and targeted analytical controls in chili and related products [10–12]. Regulation (EC) No 669/2009 was subsequently repealed by Commission Implementing Regulation (EU) 2019/1793. However, the problem is broader than Sudan dyes alone. Analytical screening must therefore address both non-authorized dyes and undeclared or inappropriate use of authorized colorants.

Official control of synthetic dyes in spices is commonly based on targeted chromatographic methods, often coupled with mass spectrometric detection, because these methods provide high selectivity and confirmatory power [6,7]. Such workflows are essential for regulatory confirmation, but they are not always optimal for rapid screening of large sample numbers. Vibrational and optical spectroscopies provide a complementary route because they can measure powdered samples rapidly, non-destructively, and with little or no sample preparation [13–18]. Near-infrared spectroscopy records overtone and combination bands mainly associated with C–H, O–H, and N–H vibrations, while the visible extension captures electronic absorption of chromophores [16–18]. This is relevant for paprika adulteration because the visible region directly reflects colorant absorption, while the near-infrared (NIR) region contains information on both the dye and the paprika matrix. With suitable preprocessing and multivariate modeling, NIR and visible-near-infrared (Vis-NIR) spectroscopy can, therefore, provide rapid quantitative screening of dye-spiked paprika powders [13–15,19–23]. Previous work on *Rosmarini folium* also showed that NIR/ATR-IR quantification can be strengthened by quantum-chemical interpretation of the target compound bands [24].

Previous studies have demonstrated the potential of spectroscopic methods for paprika authentication. NIR spectroscopy has been applied to the detection of substitution adulteration, including spent paprika and cereal fillers, and to geographical or quality-related authentication of paprika powders [8,19,20,25]. Raman spectroscopy, Raman hyperspectral imaging, and surface-enhanced Raman spectroscopy (SERS) have been used to detect Sudan dyes and related color adulterants in paprika or chili matrices [26–29]. Ultraviolet–visible (UV-Vis) spectroscopy and Fourier-transform infrared (FT-IR) spectroscopy have also been explored for dye detection or paprika color assessment [30–32], while broader reviews identify NIR, mid-infrared (MIR), Raman, and hyperspectral imaging as important tools for spice authentication [13–15,33]. These studies establish the feasibility of spectroscopic

screening, but much of the paprika-focused dye literature concentrates on Sudan dyes. Recent quantitative studies used FT-NIR with PLS for Sudan II–IV and Congo red [25] and laboratory Vis-NIR with machine learning for food-dye adulteration [34]. Comparatively fewer studies address Allura Red, Orange II, and Ponceau 4R in paprika powder under a common quantitative design, and direct comparison of benchtop FT-NIR and handheld Vis-NIR remains limited [19,20,25–27,29–32,35–38]. For powdered spices, calibration design must also account for matrix heterogeneity and diffuse-reflectance scattering. Particle size, packing density, moisture, and batch-to-batch variability can change the optical path and baseline structure, often contributing variance that is not directly related to the target analyte [16–18,21]. Scatter-aware preprocessing methods such as standard normal variate (SNV), multiplicative scatter correction (MSC), and extended multiplicative signal correction (EMSC) were developed to reduce multiplicative and additive effects in NIR spectra and are widely used in quantitative spectroscopy of powders [22,23]. In portable or handheld measurements, additional constraints arise from reduced optical throughput, lower spectral resolution, spectral-range differences, and sensitivity to sample presentation [16–18,21]. For this reason, robust validation requires more than a single calibration set: it should include independent test-set validation (TSV), randomized measurements, and matrix variation representative of realistic paprika samples. A recent handheld LIBS study examined the same three sodium-salt azo dyes in paprika powder under a closely matched concentration and validation design, with the quantitative response dominated by sodium emission from the dye counter-ions [39].

Against this background, the advance of the present work is the combination, within one common quantitative design, of three azo dyes not commonly evaluated together, direct measurement of the same prepared samples by benchtop FT-NIR and handheld Vis-NIR, evaluation of the quantitative prediction performance using these techniques, and dye-specific interpretation of the PLS-relevant NIR regions supported by anharmonic calculations. Accordingly, the aim of this work is a targeted quantitative screening approach for predefined azo dyes in paprika, with emphasis on predictive performance, portability, and chemically interpretable modeling.

Here, we investigate the quantification of three representative azo dyes—Allura Red (E129), Orange II, and Ponceau 4R (E124)—in paprika powder using benchtop FT-NIR and handheld Vis-NIR spectroscopy under a common experimental design. Paprika was spiked from 0 to 6% (w/w), 17 concentration levels, 3 independently prepared batches, randomized measurements over approximately 3 months, and replicate acquisitions. Spectra were evaluated by principal component analysis (PCA) and partial least squares (PLS) regression with cross-validation and independent test-set validation (TSV). In addition to comparing predictive performance, the study uses dye-specific spectral interpretation supported by anharmonic NIR simulations to examine whether the regression models are driven by chemically plausible spectral regions. The study therefore aimed to compare the quantitative performance of benchtop FT-NIR and handheld Vis-NIR for these three dyes and to determine whether the spectral information used by the PLS models was chemically interpretable.

2. Materials and Methods

2.1. Materials

Commercial sweet paprika powder (“Paprika edelsüß spezial”, Kotányi, Wolkersdorf im Weinviertel, Austria) was used to minimize between-brand matrix variability. Three production charges were procured in April–May 2024 and labeled I–III: I (exp. 11 June 2024, lot L 419278201034; 1 retail pack), II (exp. 6 March 2025, lot L 432911131611; 5 retail packs), and III (exp. 6 March 2025, lot L 432911131603; 1 retail pack); each retail pack contained

250 g. After opening, paprika was stored sealed and protected from ambient light until sample preparation. Light-protected 50 mL brown polypropylene centrifuge tubes (Falcon, London, UK) were used for weighing/mixing and storage of spiked paprika batches (total 8 g per tube). For FT-NIR/Vis-NIR measurements, cylindrical optical-glass reflection cells (Hellma Analytics, Baden-Württemberg, Germany, type 692.091-OG, Art. No. 692-091-12) were filled with ~2 g powder and compressed and leveled with a stainless-steel clamp to obtain a flat and reproducible surface.

Three azo dyes were selected as representative water-soluble colorants: Allura Red (E129), Orange II (non-authorized food colorant), and Ponceau 4R (E124). Specifications are summarized in Table 1 and chemical structures are shown in Figure 1.

Table 1. Specifications of all three colorants.

Colorant	Allura Red	Orange II	Ponceau 4R
E number	E129	-	E124
CAS no.	25956-17-6	633-96-5	2611-82-7
Molecular formula	$C_{18}H_{14}N_2Na_2O_8S_2$	$C_{16}H_{11}N_2NaO_4S$	$C_{20}H_{11}N_2O_{10}S_3Na_3$
Molar mass/g·mol^{-1}	496.42	350.32	604.47
Manufacturer	Roth	Fisher Scientific/ Thermo Scientific	Roth
Charge	214354299	416561000	154353931
Purity	purest (dye content > 80%)	certified (supplier)	purest (supplier)
λ_{max} (aqueous, UV-Vis)/nm	~504	~484	~507
Pack size/g	100	100	100

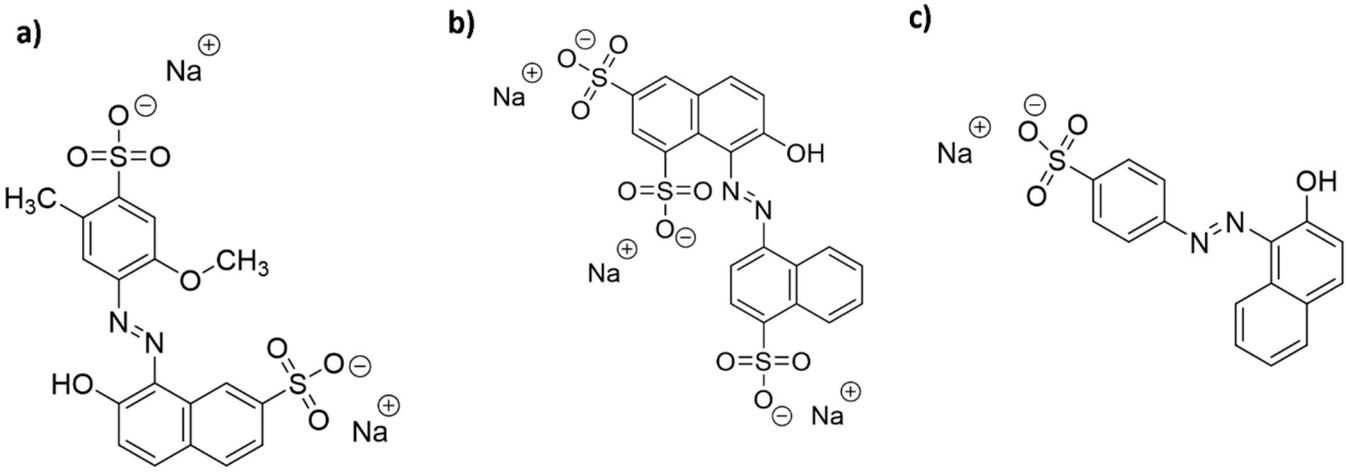

Figure 1. Structure of all three colorants (**a**) Allura Red, (**b**) Ponceau 4R, (**c**) Orange II.

2.2. Sample Preparation

Paprika powder was spiked with three azo dyes—Allura Red (E129), Orange II, and Ponceau 4R (E124)—to yield 17 concentration levels from 0 to 6% (*w*/*w*). For each dye, all 17 levels were prepared independently in triplicate (3 separately prepared batches), 8.00 g per tube, thoroughly mixed by stirring with a spatula in light-protected 50 mL brown polypropylene centrifuge tubes (Falcon), and sealed until analysis. A fixed 70:30 calibration–validation design was applied, using 12 concentrations for calibration (0, 0.10, 0.25, 0.75, 1.00, 1.50, 2.00, 3.00, 3.50, 4.50, 5.00, 6.00%) and 5 for independent test-set validation (0.50, 1.25, 2.50, 4.00, 5.50%). The 0–6% range was selected as a low-to-moderate concentration

interval with dense representation at the low end, where quantitative screening is analytically more demanding. Concentrations are reported as nominal % *w*/*w* values based on the weighed dye material as received. No correction for dye-content purity was applied unless stated otherwise. Measurements were randomized and distributed over approximately three months to reduce confounding between concentration level and day-to-day laboratory or instrumental variation. For FT-NIR and Vis-NIR measurements, approximately 2 g of powder was transferred to an optical glass cuvette, compressed and leveled with the same stainless-steel clamp to obtain a flat, reproducible surface, measured first on the benchtop FT-NIR system and then immediately on the handheld Vis-NIR system without refilling the cuvette. No drying, milling, or sieving was applied before FT-NIR/Vis-NIR measurement, preserving the minimal-preparation workflow intended for handheld/on-site use; this represents a setting that is more challenging and informative for practical application. Three replicate spectra were recorded from each filled cuvette. Thus, each concentration level and dye yielded nine raw spectra in total, originating from three independently prepared batches with three replicate acquisitions per filled cuvette. To exclude pre-contamination, attenuated total reflection infrared (ATR-IR) spectra of the unspiked paprika (each production charge) and of each neat dye were acquired prior to spiking.

2.3. Spectroscopic Measurements

ATR-IR prescreening. ATR-IR was used as a prescreening step to confirm that the unspiked paprika matrix (each production charge) contained no detectable dye signatures prior to spiking and to document the neat dye spectra for comparison. Spectra were acquired on a PerkinElmer Spectrum 400 equipped with a ZnSe ATR crystal (single-reflection). Before each measurement, a background spectrum was recorded on the clean crystal; the crystal was cleaned between samples (acetone). Spectra were collected in the range 4000–650 cm^{-1} at 2 cm^{-1} resolution using 32 scans. Spiked paprika mixtures were not analyzed by ATR-IR.

FT-NIR (benchtop). Diffuse-reflectance spectra were acquired on a Büchi NIRFlex N-500 Fourier-transform near-infrared (FT-NIR) spectrometer using the "solids" cell with XL adapter (10,000–4000 cm^{-1}; 1000–2500 nm). The instrument is equipped with a tungsten–halogen source, an InGaAs detector, a quartz polarization interferometer (double TeO_2 wedges), and an internal HeNe laser reference (633 nm). Instrument referencing was performed using the internal gold reference and an external Spectralon standard. Spectra were collected at a nominal resolution of 8 cm^{-1} (constant in wavenumber units over the operational range) with 64 scans averaged, yielding 1501 data points per spectrum. Three replicate spectra were recorded per filled cuvette.

Vis-NIR (handheld). Diffuse-reflectance spectra were recorded on an ASD QualitySpec Trek (Malvern Panalytical; 28,570–4000 cm^{-1}, 350–2500 nm) equipped with a tungsten–halogen source and two detector modules (Si CCD/CMOS for the visible region and InGaAs for the NIR region). Spectra were recorded with 2151 data points at a nominal resolution of 3–10 nm throughout its operational wavelength range. For comparison with the benchtop FT-NIR instrument, 10 nm corresponds approximately to 40–45 cm^{-1} at 1500 nm, 25 cm^{-1} at 2000 nm, and 16 cm^{-1} at 2500 nm. Reflectance referencing used the internal white-reference routine (as per manufacturer workflow) and external Spectralon reference scans (Spectralon cap). Immediately after FT-NIR acquisition, the same filled cuvette was measured on the handheld Vis-NIR without refilling, and three replicate spectra were recorded per sample. For Vis-NIR modeling, the spectral range was restricted to 490–2500 nm (20,408–4000 cm^{-1}) to avoid the lower-wavelength edge region of the handheld visible detector and retain the stable visible/NIR response used for modeling. The broad azo-dye absorption envelopes extended into this retained range.

All measurements were performed at ambient laboratory conditions; white/reference scans were repeated regularly during each session to minimize instrumental drift.

2.4. Data Pretreatment and Chemometrics

For FT-NIR and Vis-NIR, diffuse reflectance spectra (R) were converted to absorbance units as log(1/R). The three consecutively recorded instrumental replicate spectra from each filled cuvette were retained as individual observations in the final models. The three independently prepared spiked batches at each concentration level were retained as separate sample groups, and all replicate spectra from the same independently prepared sample were kept together during grouped cross-validation to prevent replicate leakage. Preliminary pretreatment screening was performed on representative batch-level models using SNV, detrending, Savitzky–Golay (SG) first derivative, and SG second derivative preprocessing. All tested pretreatments yielded good prediction performance. SNV was selected for the final workflow because it provided consistently strong models while preserving the broad spectral features relevant for interpretation of diffuse-reflectance NIR and Vis-NIR spectra. SNV was followed by mean-centering before PCA and PLS regression. PCA was used for exploratory analysis of sample structure, and PLS regression was used for quantitative modeling. The predefined 12 concentration levels were used for calibration, and the remaining 5 levels were held out for independent test-set validation (70:30 split) based on held-out concentration levels; no spectra from held-out concentration levels were used at any stage of model fitting. The number of latent variables (LVs) in PLS was selected within the calibration set by grouped cross-validation, with all replicate spectra from the same independently prepared sample kept together within each cross-validation segment.

Model performance was assessed using the root-mean-square error of calibration (RMSEC); root-mean-square error of cross-validation (RMSECV); root-mean-square error of prediction for the independent test set (RMSEP); and the corresponding coefficients of determination for calibration, cross-validation, and test-set validation (R^2_{cal}, R^2_{CV}, and R^2_{TSV}). The residual predictive deviation for the test set (RPDTSV) was calculated as the standard deviation of the reference concentrations in the test set divided by RMSEP. Model complexity was reported as the number of LVs.

Limits of detection and quantification were additionally estimated for the final PLS models using the IUPAC-consistent multivariate framework of Allegrini and Olivieri [40]. PLS sensitivity was calculated as SEN = $1/||b||$ from the final regression coefficient vector. Minimum and maximum zero-analyte leverages were derived in the retained latent-variable space, including the 1/I correction for mean-centered data. Instrumental signal variance was estimated by pooling the within-sample variance of the three replicate spectra after the same log(1/R) and SNV preprocessing used for modeling. The mLOD interval was calculated using a factor of 3.3 and the mLOQ interval using a factor of 10 in the propagated zero-analyte prediction uncertainty. The propagated reference-concentration uncertainty estimated from the analytical-balance readability was approximately 0.00122% *w*/*w* and changed the resulting mLOD values by less than 0.1% relative; this contribution was therefore negligible in the reported values (Table S3).

All chemometric analyses were performed in Unscrambler X 10.5 (CAMO Software AS, Oslo, Norway), and figures were prepared in OriginPro 2024 (OriginLab Corporation, Northampton, MA, USA) and MATLAB R2020b (MathWorks, Natick, MA, USA).

2.5. Theoretical Calculations of NIR Spectra

All quantum mechanical calculations were performed with Gaussian 16 Rev. C02 software [41]. Theoretical NIR spectra were obtained from fully anharmonic vibrational calculations using deperturbed vibrational second-order perturbation theory (DVPT2) as

implemented in Gaussian [42,43]. The calculations used the corresponding sulfonic-acid forms of all three dyes. For each dye (Allura Red, Ponceau 4R, Orange II), a geometry optimization was carried out at the density functional theory (DFT) level (B3LYP/6-31G(d,p)) including the D3 dispersion correction of Grimme with Becke–Johnson damping (GD3BJ; D3 parametrization) [44,45]. Very tight geometry-convergence criteria and a SuperFine integration grid were applied. All optimized structures were confirmed as minima by the absence of imaginary harmonic frequencies. The self-consistent field (SCF) equations were converged using the quadratically convergent SCF algorithm, together with tight integral accuracy setting. The anharmonic treatment yielded transition frequencies and intensities for non-fundamental bands relevant to the NIR region. The simulated spectra were restricted to two-quanta transitions, i.e., first overtones (2ω) and binary combination bands ($\omega_a + \omega_b$); higher-order transitions (second overtones and ternary combinations) were not included. Stick spectra were converted to continuous spectra by convolution with a parameterized band broadening function. A Lorentz–Gauss (Cauchy–Gauss) product profile was used as the bandshape model [46], with broadening parameters chosen to reproduce realistic experimental linewidths.

To support interpretation, computed transitions were additionally summarized in a mode-resolved intensity map ("assignment heatmap"), which visualizes how groups of vibrations contribute to the overall NIR lineshape (an approach commonly used in fully anharmonic NIR simulation work [47,48]). All spectral post-processing and visualization (stick-to-profile convolution, simulated spectra plots, and heatmap generation) were performed in MATLAB (MathWorks, Natick, MA, USA).

3. Results and Discussion

3.1. Spectral Characterization of Paprika and Colorants

ATR-IR prescreening was used as a qualitative matrix check before spiking. Spectra of the three unspiked paprika charges were compared with spectra of the neat dyes, Allura Red, Orange II, and Ponceau 4R (Figure S1). The neat dyes showed pronounced bands in the ~1525–1460 cm^{-1} region, assigned to coupled azo/aromatic ring vibrations, together with intense sulfonate-related bands in the ~1250–1150 cm^{-1} region and broad OH/NH contributions around ~3500–3200 cm^{-1}. In contrast, paprika was dominated by aliphatic CH_2/CH_3 stretching bands near ~2920 and ~2850 cm^{-1} and by carbohydrate/lipid C–O contributions in the ~1150–1000 cm^{-1} region. No dye-characteristic bands were observed in the unspiked paprika charges, indicating that the selected dyes were not detectable above the sensitivity of this ATR-IR screening. ATR-IR was therefore used only to exclude obvious pre-contamination and to document reference signatures of the neat dyes, not as a quantitative method.

Figure 2 compares the NIR spectra of neat paprika and the neat dye powders. The paprika matrix showed the expected OH- and CH-dominated diffuse-reflectance profile, including water-associated bands near ~6900 cm^{-1} and ~5235 cm^{-1} [47,49] (discussed further below), together with CH overtone and combination-band contributions in the ~6100–4500 cm^{-1} region [50,51]. The matrix bands form the main spectral background against which dye-related changes in the mixtures must be interpreted. The neat dyes showed weaker water-related bands than paprika, but displayed broader dye-related features in the CH overtone and combination-band region, especially near ca. 6000 cm^{-1} and below ca. 5200 cm^{-1}. A broader assignment of paprika matrix bands is provided in Table S1.

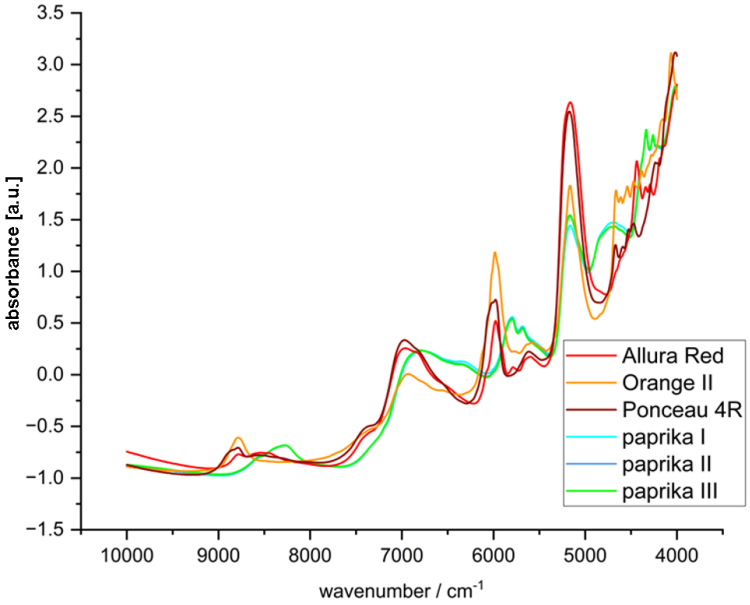

Figure 2. NIR spectra of pure paprika and pure colorants.

Azo dyes can be hygroscopic or retain residual moisture; however, in this work, the dyes were deliberately used as received and were not dried, because a practical adulteration scenario would most likely not include such a step. The neat dye powders were instead monitored in an open cuvette over 24 h. Residual OH- and hydration-related contributions were visible in the NIR spectra of the raw dyes, especially in the typical regions near ca. 6900 and 5235 cm^{-1} (Figure 2). However, no systematic increase in these features was observed during the monitoring period. Therefore, the concentration-dependent spectral changes in the spiked paprika mixtures were not attributed to progressive moisture uptake during handling.

In the spiked paprika series, the most informative NIR changes occurred between ca. 6100 and 4500 cm^{-1} (Figure 3). For all three dyes, increasing concentration produced systematic changes in this region, especially around 6000 cm^{-1} and in the crowded 5200–4700 cm^{-1} region. The ~6000 cm^{-1} region contains contributions from the aromatic C–H first overtone of the dye structures, while the lower-wavenumber interval overlaps with dense combination-band contributions from both dyes and paprika. Orange II showed the clearest dye-specific NIR features, including distinct contributions around 5980 cm^{-1} and in the higher-wavenumber NIR region, whereas Allura Red and Ponceau 4R were less distinct from the paprika matrix in the NIR window. This difference is relevant for the PLS behavior discussed in Section 3.2.

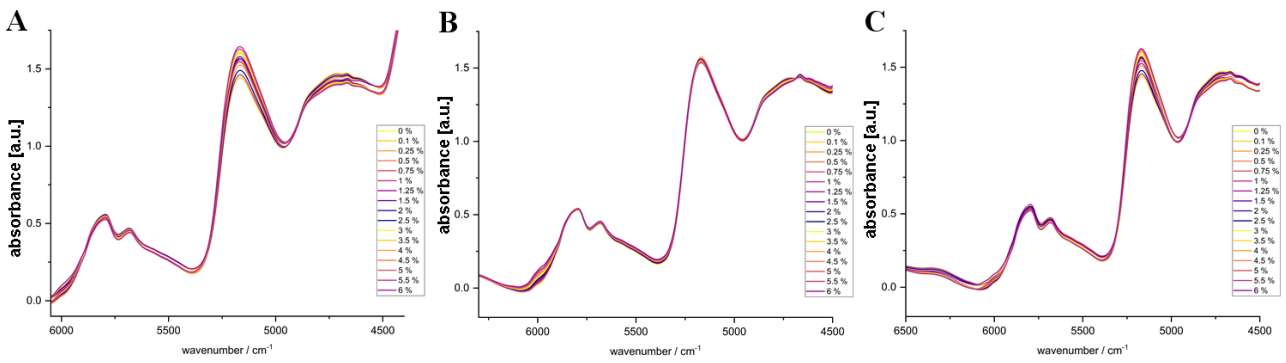

Figure 3. NIR spectra of paprika powder with different concentrations of (**A**) Allura Red batch 1, (**B**) Orange II batch 1, (**C**) Ponceau 4R batch 1, zoomed into the region 6000–4500 cm^{-1}.

To support the experimental interpretation, calculated anharmonic NIR spectra were evaluated using mode-resolved DVPT2 heatmaps. The three dyes showed the same general structure of aromatic C–H overtone intensity and dense lower-wavenumber combination-band contributions, with dye-specific differences summarized in Table 2. The simulations indicate that the dominant dye-related NIR intensity arises from aromatic C–H first overtones near ca. 6100–5850 cm^{-1} and from dense binary combination-band manifolds below ca. 5200 cm^{-1} (Figures 4–6). These combination bands involve C–H stretching coupled with ring deformations, C–C–H bending modes, and dye-dependent heteroatom vibrations, including sulfonate-related S–O/S–O–H contributions. Orange II additionally shows an explicit N–N-labeled contribution in the lower-wavenumber combination-band region. The main simulation-supported dye regions and their relevance to the paprika mixtures are summarized in Table 2. The calculations represent isolated molecular structures, which are sufficient for qualitative assignment of overtone and combination-band vibrational structure; discrepancies in band positions or linewidths result from solid-state characteristics. These effects primarily include intermolecular hydrogen bonding and local hydration of sulfonate/hydroxyl groups, resulting in the observed redshift of O–H/N–H transitions (mostly observed at ca. 7000–6500 cm^{-1}), band broadening and redistributed intensity within grouped combination bands at lower wavenumbers (ca. 5000–4000 cm^{-1}), as seen in Figures 4–6.

Table 2. Representative NIR bands of the azo dyes (Allura Red, Orange II, Ponceau 4R) supported by DVPT2 anharmonic calculations.

Representative Region/cm^{-1}	Wavelength Region/nm	Dominant Contribution (DVPT2 Heatmap)	Notes
7200–6800	1389–1471	νO–H first overtone	Present in the simulations, but experimentally weak in dry dye powders compared with paprika water/OH bands.
6550–6250	1527–1600	νO–H overtone component (strongly hydrogen bonded); contribution of νC-H first overtones and binary combinations toward lower wavenumbers	Most evident for Orange II; less pronounced for Allura Red and Ponceau 4R.
6100–5850	1639–1710	Aromatic νC-H first overtones and binary combinations	Main dye-sensitive overtone region; increases systematically with dye fraction in the mixtures.
5850–5600	1710–1786	νC–H overtones from substituted aromatic or alkyl environments	Contributes to shape differences between paprika and dyes in the ~5800–6000 cm^{-1} region.
5100–4700	1961–2128	νO–H/νC–H combination band	Overlaps with paprika water and carbohydrate contributions; changes should be interpreted as dye effects in a crowded matrix region, not as a pure water marker.
4700–4000	2128–2500	νC–H + δring combinations, with sulfonate-related and dye-specific heteroatom contributions	Region with the clearest simulated dye-specific structure; Orange II shows N–N-labeled contributions, while Allura Red and Ponceau 4R show stronger sulfonate-related rows.

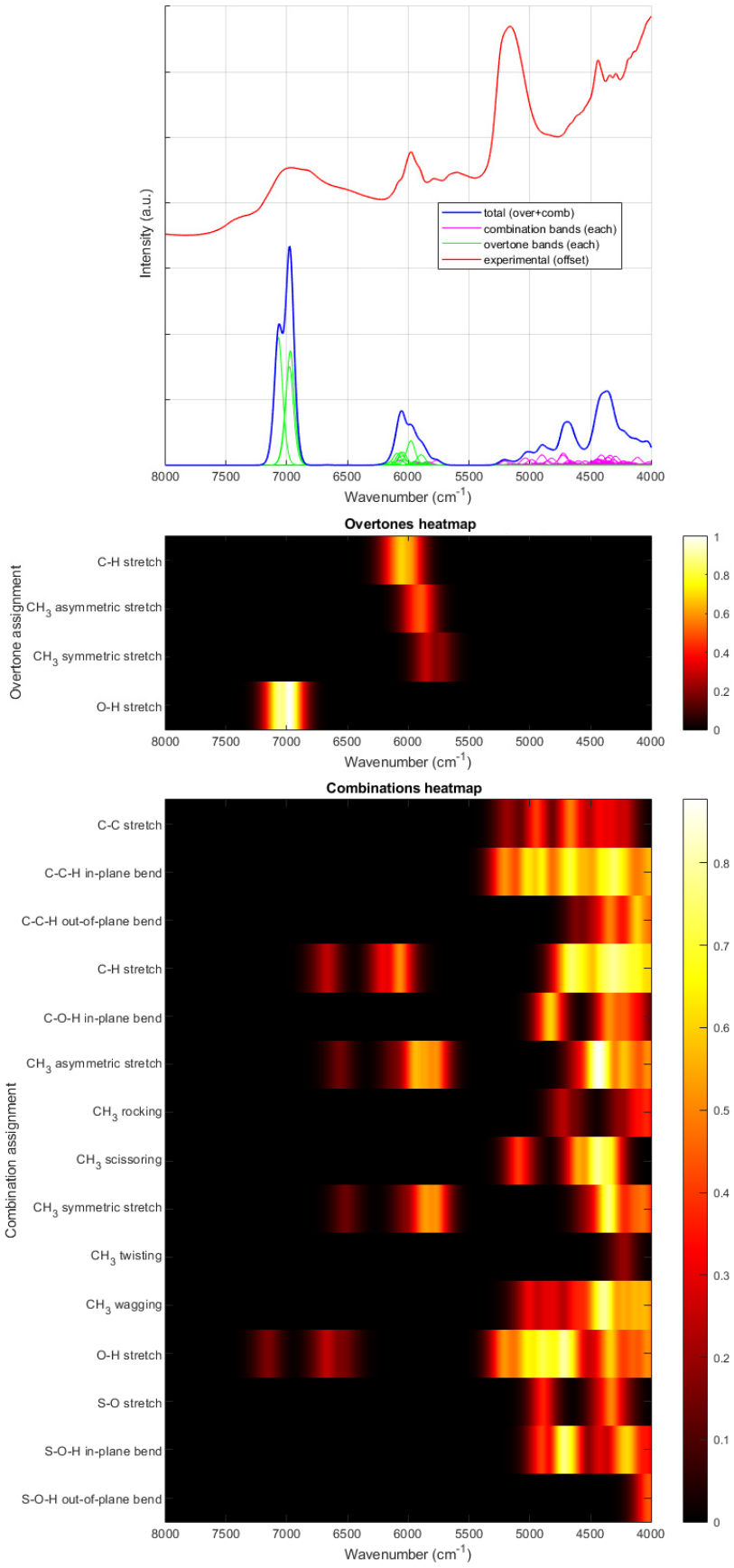

Figure 4. Mode-resolved band-assignment heatmap for Allura Red from DVPT2 anharmonic calculations, overtone (2ω) and binary combination (ω_a + ω_b) contributions to the simulated NIR spectrum.

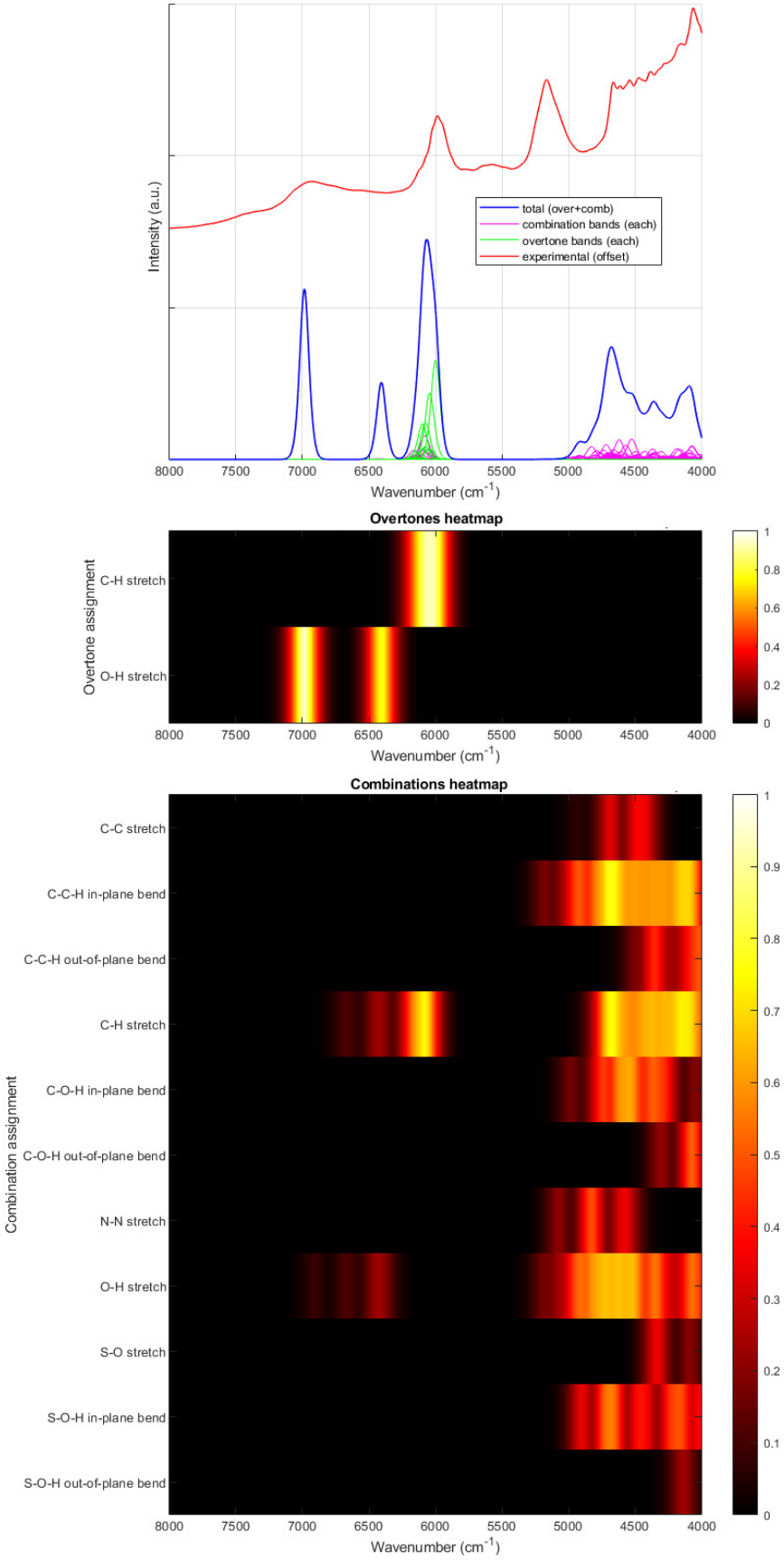

Figure 5. Mode-resolved band-assignment heatmaps for Orange II from DVPT2 anharmonic calculations; visualized are overtone (2ω) and binary combination ($\omega_a + \omega_b$) contributions to the simulated NIR spectra.

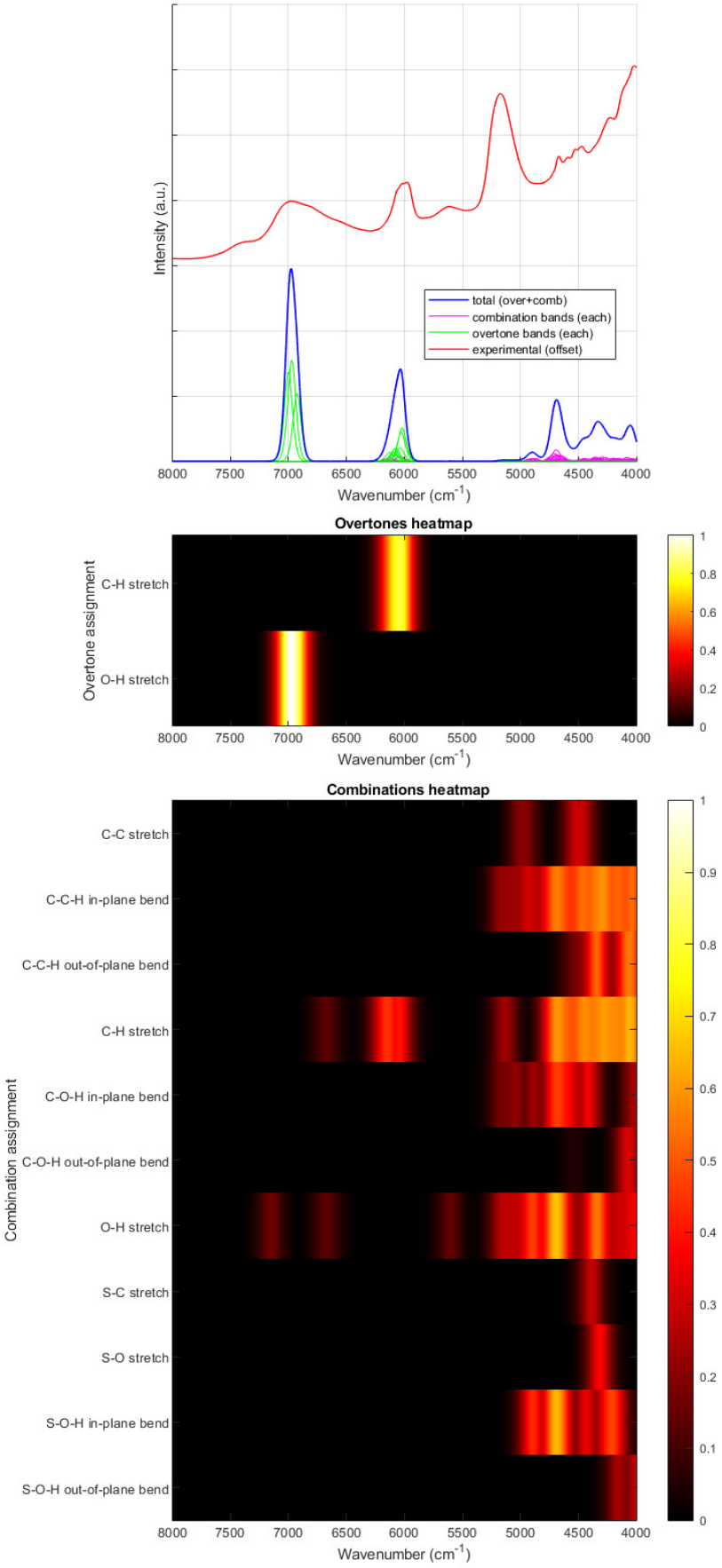

Figure 6. Mode-resolved band-assignment heatmaps for Ponceau 4R from DVPT2 anharmonic calculations; visualized are overtone (2ω) and binary combination (ω_a + ω_b) contributions to the simulated NIR spectra.

Figure 7 shows the Vis-NIR spectra of neat paprika and the neat dyes. Paprika showed a broad visible absorption envelope in the blue–green region, with the main contribution around ~470–510 nm and a longer-wavelength shoulder extending toward ~520–580 nm. This profile is consistent with carotenoid absorption in *Capsicum annuum*, mainly from capsanthin, capsorubin, and related carotenoids [52–55]. The three azo dyes showed stronger and more dye-specific visible absorption associated with the azo–aromatic chromophore. Reported aqueous absorption maxima are approximately 504 nm for Allura Red [56], 507 nm for Ponceau 4R [57], and 484 nm for Orange II [58], with exact positions depending on solvent and pH. In diffuse-reflectance powder spectra, these bands broaden and may shift relative to solution spectra, but they remain sufficiently pronounced to provide direct visible-region information for PLS modeling. This is reflected here by the lower complexity of the Vis-NIR models, especially for Allura Red and Ponceau 4R.

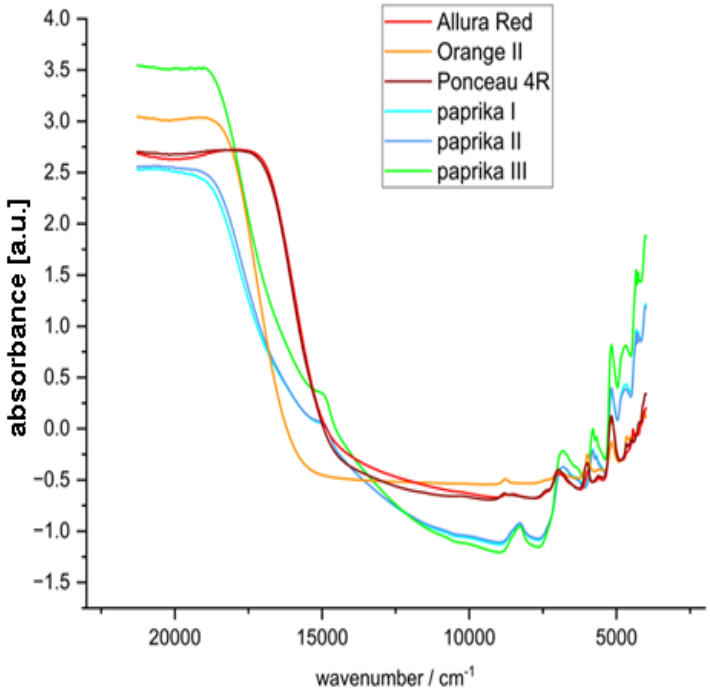

Figure 7. Vis-NIR spectra of the pure paprika and pure colorants.

3.2. PCA Models

PCA was used as an unsupervised check of the dominant variance structure before PLS modeling. Its purpose was not class assignment, but to verify whether concentration-related spectral variance dominated over secondary matrix/sample-presentation effects and to identify potentially anomalous structure before supervised regression. For the NIR data, the SNV-pretreated log(1/R) spectra showed a clear concentration-related ordering in the score space (Figure 8a). In the Allura Red series, the first two PCs explained more than 95% of the spectral variance. The main score trend followed dye concentration, while PC2 retained a weaker contribution from paprika production charge and associated baseline/scattering differences. This secondary matrix contribution was most evident in the early subset of measurements and became less pronounced after inclusion of the full set of concentration levels and independently prepared batches. Similar PCA behavior was observed for Orange II and Ponceau 4R, with concentration ordering as the primary trend and weaker matrix-related variation as a secondary component (Figures S2 and S3).

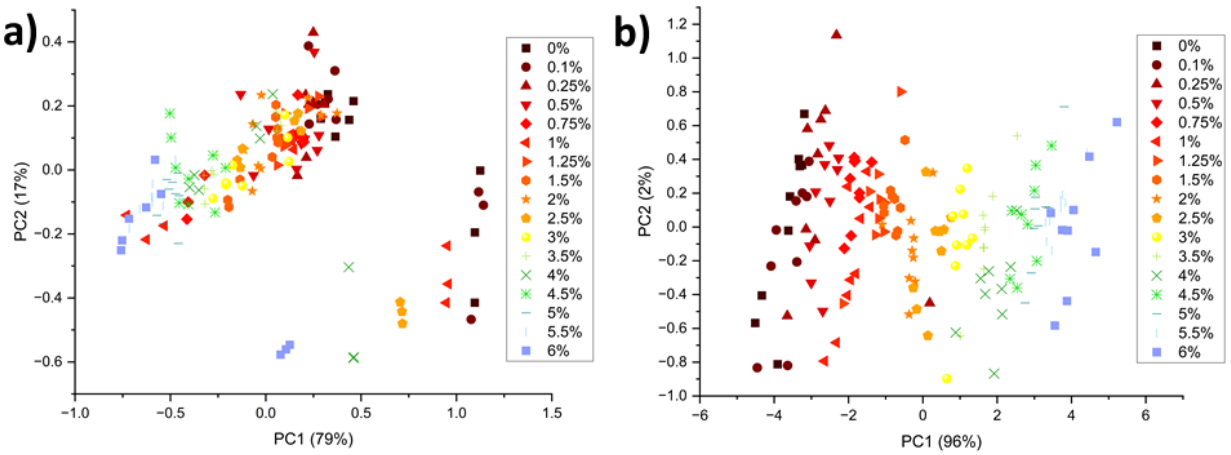

Figure 8. PCA of paprika powder with Allura Red based on: (**a**) NIR spectra, (**b**) Vis-NIR spectra.

For the handheld Vis-NIR data, the PCA structure was more compact: approximately 96% of the variance was captured by PC1 and about 2% by PC2 for the dye series. This stronger first-component dominance corresponds to the intense visible absorption of the azo chromophores, which contributes a direct concentration-dependent spectral response. The Vis-NIR scores therefore showed a clearer concentration gradient and a weaker apparent influence of paprika charge than the NIR scores (Figure 8b). The corresponding Orange II and Ponceau 4R PCA results are provided in Figures S4 and S5.

3.3. PLS Regression Models

PLS regression models were then developed separately for each dye and spectral region (Table 3). For the benchtop FT-NIR region from 10,000 to 4000 cm^{-1}, the models required only two to three latent variables. Calibration and cross-validation errors were very similar, with RMSEC/RMSECV values of 0.224/0.242% for Allura Red, 0.186/0.193% for Orange II, and 0.338/0.354% for Ponceau 4R. This close agreement indicates that the selected model complexity was adequate and does not suggest pronounced overfitting. The independent test-set validation confirmed the same trend, with RMSEP values of 0.315, 0.205, and 0.338% and R^2_{TSV} values of 0.970, 0.987, and 0.965 for Allura Red, Orange II, and Ponceau 4R, respectively. Orange II therefore gave the strongest FT-NIR model, as it contains more distinct NIR features observed for this dye in the neat spectra and in the concentration series.

Table 3. PLS regression performance for quantification of Allura Red, Orange II, and Ponceau 4R in paprika powder using NIR and Vis-NIR spectra. Errors are given in % *w*/*w*.

Wavenumber Range/cm^{-1}	Dye	LVs	RMSEC	R^2_{cal}	RMSECV	R^2_{CV}	RMSEP	R^2_{TSV}	RPDTSV
FT-NIR 10,000–4000	Allura Red	3	0.224	0.987	0.242	0.985	0.315	0.970	5.97
	Orange II	2	0.186	0.991	0.193	0.991	0.205	0.987	9.17
	Ponceau 4R	3	0.338	0.971	0.354	0.969	0.338	0.965	5.56
Vis-NIR 20,408–4000	Allura Red	2	0.274	0.981	0.298	0.979	0.328	0.968	5.73
	Orange II	3	0.355	0.967	0.381	0.964	0.262	0.979	7.18
	Ponceau 4R	2	0.348	0.969	0.379	0.965	0.334	0.964	5.63

For the Vis-NIR region from 20,408 to 4000 cm^{-1}, the Allura Red and Ponceau 4R models used two latent variables, whereas the Orange II model used three. The calibration and cross-validation statistics again remained closely matched, with RMSEC/RMSECV values of 0.274/0.298% for Allura Red, 0.355/0.381% for Orange II, and 0.348/0.379% for Ponceau 4R. Independent test-set validation gave RMSEP values of 0.328, 0.262, and 0.334% and R^2_{TSV} values of 0.968, 0.979, and 0.964 for Allura Red, Orange II, and Ponceau 4R, respectively. Thus, the Vis-NIR models provided high test-set prediction performance with uniformly low model complexity. This behavior corresponds well with the spectral interpretation in Section 3.1; the visible region provides a strong chromophore-related response for the azo dyes, while the NIR extension contributes complementary spectral information, and Orange II also exhibits comparatively distinct NIR features.

The test-set RPD values ranged from 5.56 to 9.17 (Table 3), supporting quantitative prediction performance for all dye- and instrument-specific models within the tested 0–6% *w*/*w* concentration range. This range represents the validated quantitative interval of the present proof of concept and should not be interpreted as an upper bound on adulteration encountered in practice. The design deliberately emphasized the analytically more demanding low end, with five nonzero concentration levels at or below 1% *w*/*w*, including the independently held-out 0.50% level. Extending the upper concentration range could increase range-dependent global statistics such as R^2 without providing stronger evidence for low-level screening performance. Interestingly, the comparable test-set performance of the two systems indicates that dye-related variance was captured in both the visible/electronic and NIR/vibrational regions, rather than being restricted to a single spectral mechanism.

The Allegrini–Olivieri calculation yielded model-specific mLOD intervals of 0.098–0.127% *w*/*w* for FT-NIR and 0.035–0.129% *w*/*w* for Vis-NIR; the corresponding mLOQ intervals were 0.296–0.385% *w*/*w* and 0.107–0.391% *w*/*w*, respectively (Table S2). The model-specific sensitivities, pooled within-sample replicate signal standard deviations, and effective zero-analyte leverage ranges underlying these estimates are reported in Table S3. These values are multivariate model figures of merit under the replicate-based signal-variance assumption and are not substitutes for independent low-level validation. The lowest concentration completely held out from calibration was 0.50% *w*/*w*, which was predicted directly by all six models. Concentrations below 0.50% *w*/*w* were represented in calibration but were not independently challenged; practical screening claims are, therefore, anchored to the independently validated 0.50% level rather than to the formal sub-0.50% mLOD values.

The final models used the non-averaged instrumental replicate spectra with grouped cross-validation, with all replicate spectra from the same independently prepared sample kept within the same validation segment. This preserves replicate-level spectral variation while preventing information leakage between model fitting and cross-validation prediction. The corresponding calibration and cross-validation regression plots are provided in Figure 9, confirming the close agreement between reference and predicted concentrations for all dye- and instrument-specific models.

The present validation outcomes can be compared with those obtained by handheld LIBS using the same paprika production charges, concentration levels, and held-out test concentrations [39]. Uniform SNV-treated LIBS models gave test-set RMSE values of 0.638–0.716% *w*/*w* and R^2_{TSV} values of 0.845–0.875 using four to five latent variables. Evaluation of dye-dependent outlier removal and variable selection gave the lowest individual test-set RMSE values of 0.517–0.716% *w*/*w*. In comparison, mean RMSEP across the three dyes was 0.286% *w*/*w* for FT-NIR and 0.308% *w*/*w* for Vis-NIR, compared with 0.688% *w*/*w* for the uniform LIBS models, and the NIR models required only two to three latent variables. These values indicate lower reported prediction errors and lower model complexity for the direct NIR measurements. The comparison refers to the complete analytical

workflows because the LIBS metrics were reported at the measurement-position level for dried, Al_2O_3-bound pellets, while the present results were obtained from non-averaged replicate spectra evaluated using grouped cross-validation of directly measured paprika powder. The LIBS study reported workflow-specific screening thresholds based on blank predictions and repeated-position averaging [39], whereas the present work reports multivariate mLOD/mLOQ values derived from the PLS models. Because the two frameworks quantify different figures of merit, their numerical limits should not be interpreted as directly equivalent detection thresholds.

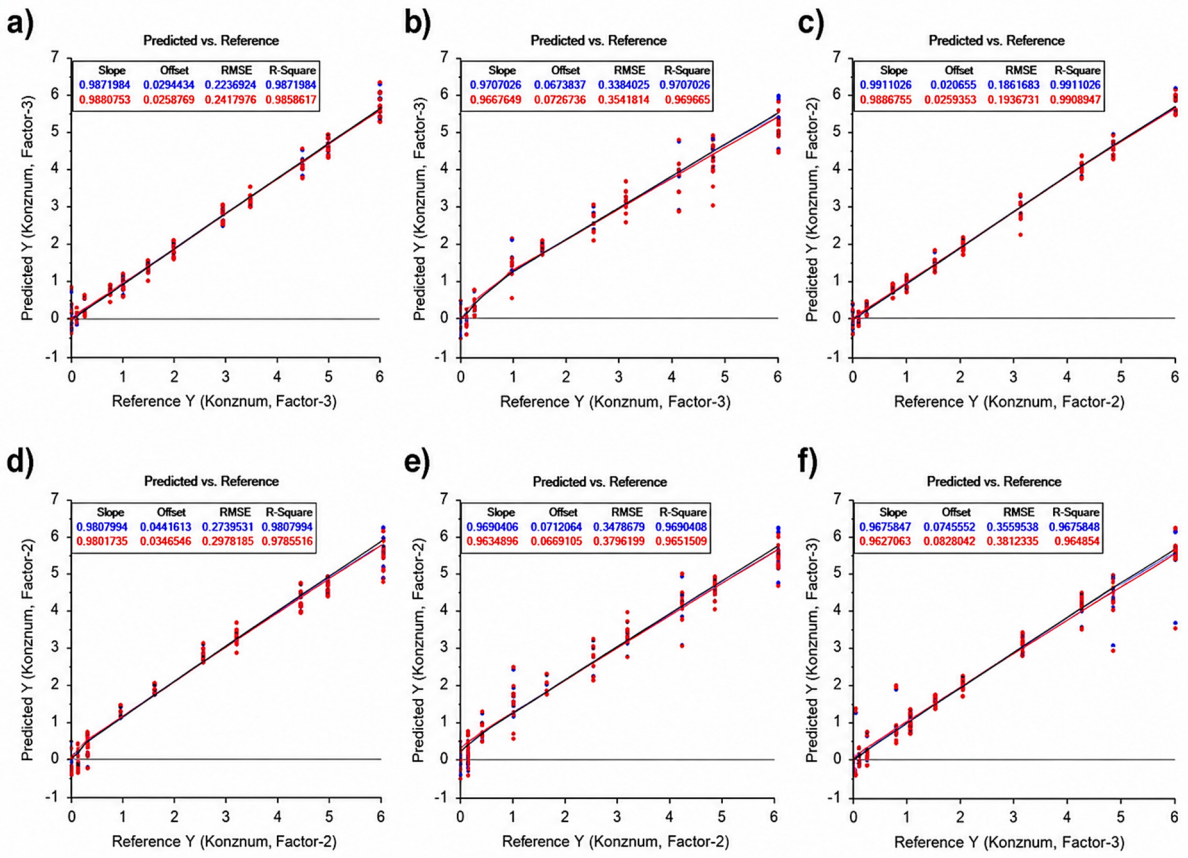

Figure 9. PLS regression plots for the quantification of azo dyes in paprika powder using FT-NIR and Vis-NIR spectra. Panels (**a**–**c**) show FT-NIR models for Allura Red, Ponceau 4R, and Orange II, respectively; panels (**d**–**f**) show the corresponding Vis-NIR models. Calibration and cross-validation predictions are shown against the reference dye concentrations.

Inspection of the PLS X-loadings further supported the different analytical mechanisms of the two spectral ranges (Figure S6). For the benchtop FT-NIR models, the dominant spectral variance associated with the regression models was located mainly in broad overtone and combination-band regions near ~6100–5850 cm^{-1} and below ~5200 cm^{-1}, in agreement with the DVPT2-supported aromatic C–H overtone and dense combination-band assignments. These regions overlap with paprika water/carbohydrate contributions, so the FT-NIR loadings are interpreted as mixed dye–matrix covariance, without evidence for isolated dye markers. Orange II showed the most distinct FT-NIR loading structure, consistent with its superior FT-NIR prediction performance, while Allura Red and Ponceau 4R showed stronger contribution from broader matrix-overlapped regions. In contrast, the most pronounced loading structures of the handheld Vis-NIR models occurred in the visible absorption region of the azo chromophores, explaining their uniformly low model complexity.

Particle size and absolute moisture content were not independently quantified. No additional drying, milling, or sieving was introduced before FT-NIR/Vis-NIR measurement because the intended workflow was deliberately minimal-preparation and compatible with handheld/on-site screening; extensive physical conditioning would reduce this practical advantage and could also narrow calibration variability beyond that encountered in commercial powders. Instead, sample handling and presentation were standardized through consistent mixing, fixed cell geometry, compression/leveling, immediate sequential measurement on the two instruments, and SNV preprocessing. PCA showed production-charge/matrix effects as secondary rather than dominant variance, while the PLS-relevant FT-NIR regions coincided with chemically plausible dye-related overtone and combination-band regions supported independently by the anharmonic calculations, and the Vis-NIR models were dominated by the expected azo-chromophore absorption. Together with the stable grouped cross-validation and independent test-set performance, these results show that the physical variability retained under the investigated conditions did not dominate or prevent robust quantitative prediction. Broader validation across independent commercial paprika matrices remains necessary to establish full real-world transferability.

The loading patterns did not show a monotonic relationship between the number of sulfonate groups and FT-NIR prediction performance. Orange II, which contains one sulfonate group, showed the most distinct FT-NIR loading structure, while the more highly sulfonated Allura Red and Ponceau 4R showed greater contribution from broad matrix-overlapped regions. This suggests that sulfonation mainly contributes to polarity- and hydration-related matrix covariance, while the more distinctive FT-NIR response of Orange II is associated with its aromatic/naphthol vibrational structure.

The relative performance of Orange II further illustrates the different origins of the analytical responses. Orange II gave the lowest RMSEP in both the FT-NIR and Vis-NIR datasets, while the LIBS study reported the highest workflow-specific screening threshold for this dye (1.75% w/w, compared with 0.26% w/w for Allura Red and 0.37% w/w for Ponceau 4R) [39]. This reversal is consistent with FT-NIR and Vis-NIR responding to molecular vibrational and electronic structure, respectively, while LIBS predominantly followed Na emission from the dye salts. At equal nominal dye mass, monosodium Orange II contributes less sodium than disodium Allura Red and trisodium Ponceau 4R, while its aromatic/naphthol structure provides comparatively distinct NIR features. The opposite ranking therefore supports the interpretation that the favorable Orange II performance in the present models originates from its molecular spectral characteristics rather than from inorganic counter-ion content. Differences may also reflect assay, moisture, particle size and optical strength. Although this provides a closer molecular connection to the target compounds than the Na-dominated LIBS response, the separate single-dye calibrations used here do not establish identification of an unknown dye or simultaneous quantification in mixtures. Extension to non-targeted one-class authentication would require a substantially broader authentic-paprika population and independent challenge samples representing diverse adulterants; the present dataset was not designed for that purpose.

4. Conclusions

This study demonstrates that benchtop FT-NIR and handheld Vis-NIR spectroscopy provide robust, non-destructive quantification of Allura Red, Orange II, and Ponceau 4R in paprika powder over the tested 0–6% w/w range using a deliberately minimal-preparation workflow. Independent held-out concentration-level validation gave RMSEP values of 0.205–0.338% w/w for FT-NIR and 0.262–0.334% w/w for Vis-NIR, with R^2_{TSV} values of 0.965–0.987 and 0.964–0.979, respectively, using only two to three latent variables. The handheld Vis-NIR system therefore achieved prediction performance comparable to bench-

top FT-NIR while benefiting from the strong visible absorption of the azo chromophores, whereas FT-NIR provided higher-resolution vibrational information that could be linked to chemically plausible dye-related overtone and combination regions through anharmonic simulations. The calculated mLOD/mLOQ values demonstrate good low-level model sensitivity; formal mLOD is around 0.1% *w*/*w* on average, formal mLOQ around 0.28% *w*/*w*. The dye-averaged formal mLOD was 0.112% *w*/*w* for FT-NIR and 0.073% *w*/*w* for Vis-NIR, indicating nominally better formal sensitivity for Vis-NIR; however, this difference was driven largely by Allura Red and Ponceau 4R. Overall, the results support direct FT-NIR and handheld Vis-NIR as complementary, interpretable approaches for targeted screening of azo-dye adulteration in paprika powder.

Supplementary Materials: The following supporting information can be downloaded at https://www.mdpi.com/article/10.3390/analytica7030059/s1, Figure S1: ATR-IR spectra of pure paprika and pure colorants; Figure S2: PCA of paprika powder with Orange II based on NIR spectra; Figure S3: PCA of paprika powder with Ponceau 4R based on NIR spectra; Figure S4: PCA of paprika powder with Orange II based on Vis-NIR spectra; Figure S5: PCA of paprika powder with Ponceau 4R based on Vis-NIR spectra; Figure S6: PLS X-loadings for the final NIR and Vis-NIR regression models. Panels a–c show NIR loadings for factors 1–3 for Allura Red, Orange II, and Ponceau 4R, respectively, using the benchtop FT-NIR instrument. Panels d–f show the corresponding Vis-NIR loadings for factors 1–2 using the handheld Vis-NIR instrument; Table S1: Representative NIR bands of paprika powder (diffuse reflectance); Table S2: Multivariate limits of detection and quantification (mLOD/mLOQ) for the final PLS models calculated using the Allegrini–Olivieri framework. Table S3: Intermediate quantities underlying the Allegrini–Olivieri mLOD/mLOQ calculation.

Author Contributions: Conceptualization, J.G. and K.B.B.; methodology, J.G. and K.B.B.; validation, J.G., K.B.B., and V.M.; formal analysis, J.G. and K.B.B.; investigation, J.G., K.B.B. and A.F.-L.; resources, C.W.H.; data curation, J.G., K.B.B., V.M. and A.F.-L.; writing—original draft preparation, J.G. and K.B.B.; writing—review and editing, J.G., K.B.B., V.M., A.F.-L. and C.W.H. All authors have read and agreed to the published version of the manuscript.

Funding: This research was funded in part by the Austrian Science Fund (FWF) 10.55776/V1014. For open access purposes, the author has applied a CC BY public copyright license to any author accepted manuscript version arising from this submission.

Data Availability Statement: The original contributions presented in this study are included in the article/Supplementary Materials. Further inquiries can be directed to the corresponding author.

Conflicts of Interest: The authors declare no conflict of interest.

References

1. Sawyer, W.E.; Izah, S.C. Unmasking Food Adulteration: Public Health Challenges, Impacts and Mitigation Strategies. *ES Gen.* **2024**, *4*, 1091. [CrossRef]
2. Schweiggert, U.; Kurz, C.; Schieber, A.; Carle, R. Effects of processing and storage on the stability of free and esterified carotenoids of red peppers (*Capsicum annuum* L.) and hot chilli peppers (*Capsicum frutescens* L.). *Eur. Food Res. Technol.* **2007**, *225*, 261–270. [CrossRef]
3. EFSA Panel on Food Additives and Nutrient Sources Added to Food. Scientific Opinion on the re-evaluation of Allura Red AC (E 129) as a food additive. *EFSA J.* **2009**, *7*, 1327. [CrossRef]
4. EFSA Panel on Food Additives and Nutrient Sources Added to Food. Scientific Opinion on the re-evaluation of Ponceau 4R (E 124) as a food additive. *EFSA J.* **2009**, *7*, 1328. [CrossRef]
5. European Commission. Adulteration of Herbs and Spices | Knowledge for Policy. 2025. Available online: https://knowledge4policy.ec.europa.eu/projects-activities/adulteration-herbs-spices_en (accessed on 12 November 2025).
6. European Commission. Herbs and Spices (2019–2021). 2025. Available online: https://food.ec.europa.eu/food-safety/eu-agri-food-fraud-network/eu-coordinated-actions/herbs-and-spices-2019-2021_en (accessed on 12 November 2025).

7. Maquet, A.; Lievens, A.; Paracchini, V.; Kaklamanos, G.; de la Calle, B.; Garlant, L.; Papoci, S.; Pietretti, D.; Zdiniakova, T.; Breidbach, A.; et al. *Results of an EU Wide Coordinated Control Plan to Establish the Prevalence of Fraudulent Practices in the Marketing of Herbs and Spices*; Publications Office of the European Union: Luxembourg, 2021. [CrossRef]
8. Galvin-King, P.; Haughey, S.A.; Elliott, C.T. The Detection of Substitution Adulteration of Paprika with Spent Paprika by the Application of Molecular Spectroscopy Tools. *Foods* **2020**, *9*, 944. [CrossRef]
9. Velázquez, R.; Rodríguez, A.; Hernández, A.; Casquete, R.; Benito, M.J.; Martín, A. Spice and Herb Frauds: Types, Incidence, and Detection: The State of the Art. *Foods* **2023**, *12*, 3373. [CrossRef]
10. European Parliament and of the Council. Commission Regulation (EC) No 669/2009. 2025. Available online: https://www.legislation.gov.uk/eur/2009/669/adopted/data.html (accessed on 12 November 2025).
11. Shah, D.D.; Goh, E.; Burgess, J.A. *Rapid Analysis of Sudan and Other Prohibited Dyes in Chili Powder Using the ACQUITY UPLC H-Class System with Xevo TQD*; Waters Corporation: Milford, MA, USA, 2014.
12. European Union. Regulation—669/2009—EN—EUR-Lex: Commission Regulation (EC) No 669/2009 of 24 July 2009 Implementing Regulation (EC) No 882/2004 of the European Parliament and of the Council as Regards the Increased Level of Official Controls on Imports of Certain Feed and Food of Non-Animal Origin and Amending Decision 2006/504/EC (Text with EEA Relevance). 2026. Available online: https://eur-lex.europa.eu/eli/reg/2009/669/oj/eng (accessed on 16 June 2026).
13. Lohumi, S.; Lee, S.; Lee, H.; Cho, B.-K. A review of vibrational spectroscopic techniques for the detection of food authenticity and adulteration. *Trends Food Sci. Technol.* **2015**, *46*, 85–98. [CrossRef]
14. Shawky, E.; Nahar, L.; Nassief, S.M.; Sarker, S.D.; Ibrahim, R.S. Spice authentication by near-infrared spectroscopy: Current advances, limitations, and future perspectives. *Trends Food Sci. Technol.* **2024**, *148*, 104522. [CrossRef]
15. Oliveira, M.M.; Cruz-Tirado, J.P.; Barbin, D.F. Nontargeted Analytical Methods as a Powerful Tool for the Authentication of Spices and Herbs: A Review. *Compr. Rev. Food Sci. Food Saf.* **2019**, *18*, 670–689. [CrossRef]
16. Crocombe, R.A. Portable Spectroscopy. *Appl. Spectrosc.* **2018**, *72*, 1701–1751. [CrossRef]
17. Beć, K.B.; Grabska, J.; Huck, C.W. Principles and Applications of Miniaturized Near-Infrared (NIR) Spectrometers. *Chem. Eur. J.* **2021**, *27*, 1514–1532. [CrossRef]
18. Yan, H.; De Gea Neves, M.; Noda, I.; Guedes, G.M.; Silva Ferreira, A.C.; Pfeifer, F.; Chen, X.; Siesler, H.W. Handheld Near-Infrared Spectroscopy: State-of-the-Art Instrumentation and Applications in Material Identification, Food Authentication, and Environmental Investigations. *Chemosensors* **2023**, *11*, 272. [CrossRef]
19. Oliveira, M.M.; Cruz-Tirado, J.P.; Roque, J.V.; Teófilo, R.F.; Barbin, D.F. Portable near-infrared spectroscopy for rapid authentication of adulterated paprika powder. *J. Food Compos. Anal.* **2020**, *87*, 103403. [CrossRef]
20. Monago-Maraña, O.; Eskildsen, C.E.; Galeano-Díaz, T.; La Muñoz de Peña, A.; Wold, J.P. Untargeted classification for paprika powder authentication using visible—Near infrared spectroscopy (VIS-NIRS). *Food Control* **2021**, *121*, 107564. [CrossRef]
21. Vera, D.N.; Ruisánchez, I.; Callao, M.P. Establishing time stability for multivariate qualitative methods. Case study: Sudan I and IV adulteration in food spices. *Food Control* **2018**, *92*, 341–347. [CrossRef]
22. Dhanoa, M.S.; Lister, S.J.; Sanderson, R.; Barnes, R.J. The Link between Multiplicative Scatter Correction (MSC) and Standard Normal Variate (SNV) Transformations of NIR Spectra. *J. Near Infrared Spectrosc.* **1994**, *2*, 43–47. [CrossRef]
23. Martens, H.; Stark, E. Extended multiplicative signal correction and spectral interference subtraction: New preprocessing methods for near infrared spectroscopy. *J. Pharm. Biomed. Anal.* **1991**, *9*, 625–635. [CrossRef]
24. Kirchler, C.G.; Pezzei, C.K.; Beć, K.B.; Henn, R.; Ishigaki, M.; Ozaki, Y.; Huck, C.W. Critical Evaluation of NIR and ATR-IR Spectroscopic Quantifications of Rosmarinic Acid in Rosmarini folium Supported by Quantum Chemical Calculations. *Planta Medica* **2017**, *83*, 1076–1084. [CrossRef]
25. Castell, A.; Arroyo-Manzanares, N.; López-García, I.; Zapata, F.; Viñas, P. Authentication strategy for paprika analysis according to geographical origin and study of adulteration using near infrared spectroscopy and chemometric approaches. *Food Control* **2024**, *161*, 110397. [CrossRef]
26. Haughey, S.A.; Galvin-King, P.; Ho, Y.-C.; Bell, S.E.; Elliott, C.T. The feasibility of using near infrared and Raman spectroscopic techniques to detect fraudulent adulteration of chili powders with Sudan dye. *Food Control* **2015**, *48*, 75–83. [CrossRef]
27. Monago-Maraña, O.; Eskildsen, C.E.; Afseth, N.K.; Galeano-Díaz, T.; La Muñoz de Peña, A.; Wold, J.P. Non-destructive Raman spectroscopy as a tool for measuring ASTA color values and Sudan I content in paprika powder. *Food Chem.* **2019**, *274*, 187–193. [CrossRef]
28. Di Anibal, C.V.; Marsal, L.F.; Callao, M.P.; Ruisánchez, I. Surface Enhanced Raman Spectroscopy (SERS) and multivariate analysis as a screening tool for detecting Sudan I dye in culinary spices. *Spectrochim. Acta Part A Mol. Biomol. Spectrosc.* **2012**, *87*, 135–141. [CrossRef]
29. Lohumi, S.; Lee, H.; Kim, M.S.; Qin, J.; Kandpal, L.M.; Bae, H.; Rahman, A.; Cho, B.-K. Calibration and testing of a Raman hyperspectral imaging system to reveal powdered food adulteration. *PLoS ONE* **2018**, *13*, e0195253. [CrossRef]
30. Di Anibal, C.V.; Odena, M.; Ruisánchez, I.; Callao, M.P. Determining the adulteration of spices with Sudan I-II-II-IV dyes by UV-visible spectroscopy and multivariate classification techniques. *Talanta* **2009**, *79*, 887–892. [CrossRef]

31. Di Anibal, C.; Rodriguez, M.S.; Albertengo, L. UV-Visible Spectroscopy and Multivariate Classification as a Screening Tool to Identify Adulteration of Culinary Spices with Sudan I and Blends of Sudan I + IV Dyes. *Food Anal. Methods* **2014**, *7*, 1090–1096. [CrossRef]
32. Lohumi, S.; Joshi, R.; Kandpal, L.M.; Lee, H.; Kim, M.S.; Cho, H.; Mo, C.; Seo, Y.-W.; Rahman, A.; Cho, B.-K. Quantitative analysis of Sudan dye adulteration in paprika powder using FTIR spectroscopy. *Food Addit. Contam. Part A Chem. Anal. Control Expo. Risk Assess.* **2017**, *34*, 678–686. [CrossRef]
33. Monago-Maraña, O.; Durán-Merás, I.; La Muñoz de Peña, A.; Galeano-Díaz, T. Analytical techniques and chemometrics approaches in authenticating and identifying adulteration of paprika powder using fingerprints: A review. *Microchem. J.* **2022**, *178*, 107382. [CrossRef]
34. Tmimi, Y.; Chikri, M.; Fethi, F. Rapid quantification of paprika adulteration by food dye using visible and near-infrared spectroscopy combined with machine learning. *Food Humanit.* **2025**, *5*, 100834. [CrossRef]
35. Khan, M.H.; Saleem, Z.; Ahmad, M.; Sohaib, A.; Ayaz, H.; Mazzara, M. Hyperspectral Imaging for Color Adulteration Detection in Red Chili. *Appl. Sci.* **2020**, *10*, 5955. [CrossRef]
36. Hu, Y.; Wang, S.; Wang, S.; Lu, X. Application of nuclear magnetic resonance spectroscopy in food adulteration determination: The example of Sudan dye I in paprika powder. *Sci. Rep.* **2017**, *7*, 2637. [CrossRef]
37. Fiamegos, Y.; Dumitrascu, C.; Papoci, S.; de la Calle, M.B. Authentication of PDO paprika powder (Pimentón de la Vera) by multivariate analysis of the elemental fingerprint determined by ED-XRF. A feasibility study. *Food Control* **2021**, *120*, 107496. [CrossRef]
38. Sun, X.; Zhang, M.; Wang, P.; Chen, J.; Yang, S.; Luo, P.; Gao, X. Detection and Quantitation of Adulterated Paprika Samples Using Second-Order HPLC-FLD Fingerprints and Chemometrics. *Foods* **2022**, *11*, 2376. [CrossRef]
39. Grabska, J.; Bec, K.B.; Moll, V.; Fiegl-Lechner, A.; Huck, C.W. Quantitative Screening of Sodium Salt Azo Dyes in Paprika Powder by Handheld Laser-Induced Breakdown Spectroscopy. *Analytica* **2026**, *7*, 47. [CrossRef]
40. Allegrini, F.; Olivieri, A.C. IUPAC-consistent approach to the limit of detection in partial least-squares calibration. *Anal. Chem.* **2014**, *86*, 7858–7866. [CrossRef]
41. Frisch, M.J.; Trucks, G.W.; Schlegel, H.B.; Scuseria, G.E.; Robb, M.A.; Cheeseman, J.R.; Scalmani, G.; Barone, V.; Petersson, G.A.; Nakatsuji, H.; et al. *Gaussian 16*, Revision C.02; Gaussian, Inc.: Wallingford, CT, USA, 2019.
42. Beć, K.B.; Grabska, J.; Ozaki, Y. Advances in Anharmonic Methods and Their Applications to Vibrational Spectroscopies. In *Frontiers of Quantum Chemistry*; Wójcik, M.J., Nakatsuji, H., Kirtman, B., Ozaki, Y., Eds.; Springer: Singapore, 2018; pp. 483–512. [CrossRef]
43. Beć, K.B.; Grabska, J.; Huck, C.W.; Ozaki, Y. Quantum Mechanical Simulation of Near-Infrared Spectra: Applications in Physical and Analytical Chemistry. In *Molecular Spectroscopy*; Ozaki, Y., Wójcik, M.J., Popp, J., Eds.; Wiley: Weinheim, Germany, 2019; pp. 353–388. [CrossRef]
44. Grimme, S.; Ehrlich, S.; Goerigk, L. Effect of the damping function in dispersion corrected density functional theory. *J. Comput. Chem.* **2011**, *32*, 1456–1465. [CrossRef]
45. Grimme, S.; Antony, J.; Ehrlich, S.; Krieg, H. A consistent and accurate ab initio parametrization of density functional dispersion correction (DFT-D) for the 94 elements H-Pu. *J. Chem. Phys.* **2010**, *132*, 154104. [CrossRef]
46. Pitha, J.; Jones, R.N. A comparison of optimization methods for fitting curves to infrared band envelopes. *Can. J. Chem.* **1966**, *44*, 3031–3050. [CrossRef]
47. Beć, K.B.; Grabska, J.; Badzoka, J.; Huck, C.W. Spectra-structure correlations in NIR region of polymers from quantum chemical calculations. The cases of aromatic ring, C=O, C≡N and C-Cl functionalities. *Spectrochim. Acta Part A Mol. Biomol. Spectrosc.* **2021**, *262*, 120085. [CrossRef]
48. Grabska, J.; Beć, K.B.; Mayr, S.; Huck, C.W. Theoretical Simulation of Near-Infrared Spectrum of Piperine: Insight into Band Origins and the Features of Regression Models. *Appl. Spectrosc.* **2021**, *75*, 1022–1032. [CrossRef]
49. Brülls, M.; Folestad, S.; Sparén, A.; Rasmuson, A.; Salomonsson, J. Applying spectral peak area analysis in near-infrared spectroscopy moisture assays. *J. Pharm. Biomed. Anal.* **2007**, *44*, 127–136. [CrossRef]
50. Ozaki, Y.; Wójcik, M.J.; Popp, J. (Eds.) *Molecular Spectroscopy*; Wiley: Weinheim, Germany, 2019.
51. Mecozzi, M.; Sturchio, E. Computer Assisted Examination of Infrared and Near Infrared Spectra to Assess Structural and Molecular Changes in Biological Samples Exposed to Pollutants: A Case of Study. *J. Imaging* **2017**, *3*, 11. [CrossRef]
52. Balevičius, V.; Abramavicius, D.; Polívka, T.; Galestian Pour, A.; Hauer, J. A Unified Picture of S* in Carotenoids. *J. Phys. Chem. Lett.* **2016**, *7*, 3347–3352. [CrossRef]
53. El-Tahlawy, A.S.; Samkumpim, T.; Wardani, N.I.; Kraiya, C.; Alahmad, W. Analytical advances for detecting illicit dyes in foods: Spectroscopy, chromatography, mass spectrometry, and emerging sensing techniques. *Food Chem. Toxicol.* **2026**, *207*, 115843. [CrossRef]

54. Fernández-García, E.; Carvajal-Lérida, I.; Pérez-Gálvez, A. Carotenoids exclusively synthesized in red pepper (capsanthin and capsorubin) protect human dermal fibroblasts against UVB induced DNA damage. *Photochem. Photobiol. Sci.* **2016**, *15*, 1204–1211. [CrossRef]
55. Mohd Hassan, N.; Yusof, N.A.; Yahaya, A.F.; Mohd Rozali, N.N.; Othman, R. Carotenoids of Capsicum Fruits: Pigment Profile and Health-Promoting Functional Attributes. *Antioxidants* **2019**, *8*, 469. [CrossRef]
56. Rovina, K.; Siddiquee, S.; Shaarani, S.M. Extraction, Analytical and Advanced Methods for Detection of Allura Red AC (E129) in Food and Beverages Products. *Front. Microbiol.* **2016**, *7*, 798. [CrossRef]
57. Macías-Quiroga, I.F.; Rojas-Méndez, E.F.; Giraldo-Gómez, G.I.; Sanabria-González, N.R. Experimental data of a catalytic decolorization of Ponceau 4R dye using the cobalt (II)/$NaHCO_3$/H_2O_2 system in aqueous solution. *Data Brief* **2020**, *30*, 105463. [CrossRef]
58. Pourreza, N.; Zareian, M. Determination of Orange II in food samples after cloud point extraction using mixed micelles. *J. Hazard. Mater.* **2009**, *165*, 1124–1127. [CrossRef]